



HAL
open science

Partial retention of radiogenic Pb in galena nanocrystals explains discordance in monazite from Napier Complex (Antarctica)

M.J. Turuani, A.T. Laurent, A.-M. Seydoux-Guillaume, D. Fougereuse, D. Saxey, S.M. Reddy, S.L. Harley, S. Reynaud, W.D.A. Rickard

► To cite this version:

M.J. Turuani, A.T. Laurent, A.-M. Seydoux-Guillaume, D. Fougereuse, D. Saxey, et al.. Partial retention of radiogenic Pb in galena nanocrystals explains discordance in monazite from Napier Complex (Antarctica). *Earth and Planetary Science Letters*, 2022, 588, pp.117567. 10.1016/j.epsl.2022.117567 . hal-03664891

HAL Id: hal-03664891

<https://hal.science/hal-03664891v1>

Submitted on 11 May 2022

HAL is a multi-disciplinary open access archive for the deposit and dissemination of scientific research documents, whether they are published or not. The documents may come from teaching and research institutions in France or abroad, or from public or private research centers.

L'archive ouverte pluridisciplinaire **HAL**, est destinée au dépôt et à la diffusion de documents scientifiques de niveau recherche, publiés ou non, émanant des établissements d'enseignement et de recherche français ou étrangers, des laboratoires publics ou privés.

1 Partial retention of radiogenic Pb in galena nanocrystals explains discordance in
2 monazite from Napier Complex (Antarctica)

3 Turuani M.J.^{1*}, Laurent A.T.¹, Seydoux-Guillaume A.-M.¹, Fougereuse D.^{2,3},
4 Saxey D.³, Reddy S.M.^{2,3}, Harley S.L.⁴, Reynaud S.⁵, Rickard W.D.A.³

5 ¹Univ Lyon, UJM, UCBL, ENSL, CNRS, LGL-TPE, F-42023, Saint Etienne, France

6 ²School of Earth and Planetary Sciences, Curtin University, Perth, Western Australia 6845,
7 Australia

8 ³Geoscience Atom Probe, John de Laeter Centre, Curtin University, Perth, Western Australia
9 6845, Australia

10 ⁴School of Geosciences, University of Edinburgh, Edinburgh EH9 3FE, UK

11 ⁵Univ Lyon, Université Jean Monnet, CNRS 5516, IOGS, Laboratoire Hubert Curien, F
12 42000 Saint-Étienne, France

13 **ABSTRACT**

14 The discordance of U–Th–Pb isotopic systems in geochronometers, and how such data are
15 interpreted, are still major issues in the geosciences. To better understand the disturbance of
16 isotopic systems, and how this impacts the derivation of geologically-meaningful ages,
17 previously studied discordant monazite from the ultrahigh temperature paragneiss of the
18 Archean Napier Complex (Antarctica) have been investigated. Monazite grains were
19 characterized from the micro to the nanoscale using an analytical workflow comprising laser
20 ablation inductively coupled plasma mass spectrometry (LA-ICP-MS), secondary-ion mass
21 spectrometry (SIMS), electron microprobe (EMP), transmission electron microscopy (TEM)
22 and atom probe tomography (APT). Results reveal that the least discordant monazite, hosted in

23 garnet and rutilated quartz, contain a large number of small Pb-bearing nanominerals ($\emptyset \sim 50$
24 nm) while the most discordant monazite, hosted in the quartzo-feldspathic matrix, contain a
25 smaller number of Pb-bearing nanominerals bigger in size ($\emptyset \sim 50$ to 500 nm). The degree of
26 the discordance, which was previously correlated with textural position is mechanistically
27 related to the partial retention of radiogenic Pb (Pb^*) in distinct Pb^* -bearing nanominerals (e.g.
28 PbS) within the monazite grains. *In-situ* dating (U–Pb systems with LA-ICP-MS and SIMS),
29 and isotopic information obtained by using APT ($^{207}Pb/^{206}Pb$ isotopic signature of galena and
30 $^{208}Pb/^{232}Th$ ages of the monazite matrix) allow the timing of Pb-disturbance and mobility to be
31 constrained. Results show that monazite grains crystallized at *ca.* 2.44 Ga and were affected by
32 two episodes of Pb^* mobility. The first episode (t_1) at *ca.* 1.05 Ga, led to crystallization of a first
33 generation of Pb^* -bearing nanominerals and a complete resetting of the monazite matrix at the
34 nanoscale. The second episode (t_2) at *ca.* 0.55 Ga was associated with the crystallization of a
35 second generation of Pb^* -bearing nanominerals with a $^{207}Pb/^{206}Pb$ signature indicating a mixing
36 of two Pb^* components: a component from the monazite matrix and remobilized Pb^* from the
37 first generation of Pb^* -bearing nanominerals. This second event is characterized by a more
38 localized resetting of the monazite matrix at the nanoscale compared to the t_1 event. These
39 results indicate the potential of nanoscale studies of Pb-rich nanominerals within monazite to
40 yield important details of the thermal history of complex metamorphic terranes.

41 Keywords: U–Th–Pb discordance – monazite – Pb mobility – nanogeochronology- atom
42 probe tomography

43 1. INTRODUCTION

44 Accessory mineral U–Th–Pb geochronology is widely used in Earth Sciences because the
45 existence of two U–Pb and one Th–Pb decay chains, each with different half-lives, allows direct
46 evaluation of isotopic disturbance and the accuracy of calculated dates. If the dates calculated

47 from the three decay chains differ, then the system under consideration is referred to as
48 discordant. Discordance is common in ancient and polymetamorphic rocks, where it typically
49 indicates Pb mobility or loss, and if not recognized may lead to erroneous conclusions with
50 respect to the geological history (Corfu, 2013). In situations where only one event is responsible
51 for Pb mobility, the time of Pb disturbance may be deduced by regression of discordant isotopic
52 data on graphs of $^{206}\text{Pb}/^{238}\text{U}$ vs $^{207}\text{Pb}/^{235}\text{U}$ or $^{207}\text{Pb}/^{235}\text{U}$ vs $^{208}\text{Pb}/^{232}\text{Th}$ (Allègre et al., 1974; Tera
53 and Wasserburg, 1972; Wetherill, 1963). However, multiple episodes of Pb disturbance result
54 in more complex data distributions that may be difficult to identify and reliably interpret
55 (Gebauer and Grünenfelder, 1979). This is particularly the case when the scale or mechanism
56 of Pb mobility differs between events. However, assessing the scale of Pb mobility as well as
57 the mechanisms by which Pb is disturbed, is typically difficult. The nanoscale quantification of
58 Pb distribution, coupled with isotopic analysis, has the potential to provide constraints on the
59 causes and scales of Pb mobility to yield a unique insight into the nature of discordance in the
60 U–Th–Pb isotopic systems (Peterman et al., 2016; Valley et al., 2014).

61 Fine-scale characterization of the location and behaviour of the radiogenic daughter element
62 (Pb^*) in host minerals relies on the correlation of structural observations with isotopic
63 measurements at the nanoscale. Transmission electron microscopy (TEM) has revealed Pb-rich
64 nanominerals in discordant zircon, either as native Pb (Kusiak et al., 2015) or Pb-oxide (Kusiak
65 et al., 2019). Similar features have been reported in discordant monazite (Seydoux-Guillaume
66 et al., 2003) and phase separation of Pb-enriched domains in monazite have been identified
67 through the integration of TEM and atom probe tomography (APT) analyses (Seydoux-
68 Guillaume et al., 2019). The isotopic compositions of such heterogeneities for U–Th–Pb
69 geochronometers such as zircon, monazite and rutile have been quantified using APT (Arcuri
70 et al., 2020; Blum et al., 2018; Fougèrouse et al., 2021a, 2021b, 2018; Peterman et al., 2016;
71 Seydoux-Guillaume et al., 2019; Valley et al., 2015, 2014; Verberne et al., 2020). These studies

72 typically use an advanced analytical workflow to constrain the scale of Pb mobility and the
73 timing of isolation of Pb from parental U and Th (Peterman et al., 2016; Seydoux-Guillaume et
74 al., 2019; Valley et al., 2015). This approach, which integrates textural, microstructural,
75 compositional and isotopic analyses from the micro- to the nanoscale yields significant
76 advances on the causes of isotopic discordance and ages variation at the microscale (Peterman
77 et al., 2016; Seydoux-Guillaume et al., 2018a).

78 Studies on natural zircon have demonstrated that isotopic discordance may be caused by
79 Pb* mobility associated with the annealing of radiation damage during high temperature
80 metamorphic conditions, resulting in isolated Pb* reservoirs (Kusiak et al., 2019, 2015;
81 Peterman et al., 2021, 2016; Whitehouse et al., 2017). In contrast, monazite is less sensitive to
82 the thermal history of the host rock since natural monazite remains crystalline thanks to a defect
83 recovery mechanism operating event at moderate temperature (> 180 °C; Seydoux-Guillaume
84 et al. 2018b). Pb* mobility in monazite from micro to nanoscale is promoted by fluid-assisted
85 mechanisms, such as a coupled dissolution-precipitation process (Grand'Homme et al., 2018;
86 Seydoux-Guillaume et al., 2002), and by deformation-assisted mechanisms both in fluid-
87 present (Wawrzenitz et al. 2012) and fluid-absent environments (Erickson et al., 2015;
88 Fougrouse et al., 2021b). As a result, the effects and interplay of such mechanisms, on the
89 formation and nature of nanoscale Pb* heterogeneities as well as their impact on discordance in
90 monazite cannot simply be derived from our knowledge of zircon.

91 This study re-investigates discordant monazite grains reported by Black et al. (1984) from
92 an Archean polymetamorphic granulite of the Napier Complex, East Antarctica. Multiple
93 advanced micro- to nanoscale analytical techniques are used to provide unique constraints on
94 the development and evolution of discrete Pb* reservoirs within variably-discordant monazite.
95 The integration of isotopic analyses over a range of scales is critically evaluated within the

96 context of a well-constrained metamorphic history to provide unique constraints on the
97 nanoscale mechanisms accommodating two stages of Pb-disturbance.

98 **2. METHODS**

99 Microscale imaging of monazite was conducted at 20 keV with field emission gun scanning
100 electron microscopy FEG-SEM Zeiss supra 55vp. The instrument is also equipped with an
101 energy dispersive X-ray (EDX) spectrometer.

102 Uranium–Th–Pb isotopic analyses by LA– ICP–MS were performed at the Laboratoire
103 Magmas et Volcans (Clermont-Ferrand, France). The laser ablation systems consist of a
104 Resonetics Resolution M-50E system equipped with an ultrashort pulse ATL excimer 193 nm
105 laser coupled to an Agilent 7500 cs ICP–MS. A Laser spot diameter of 9 μm was used with 1
106 Hz repetition rate and a fluence of 7.5 J/cm². The ²⁰⁴(Pb+Hg) signal was monitored but no
107 common-Pb correction was applied. Analytical procedures and reproducibility are reported in
108 detail in Appendix A. SIMS was undertaken on a CAMECA IMS 7f-Geo hosted at the NERC
109 Ion Micro-Probe Facility, School of Geosciences, Edinburgh University (UK), under conditions
110 detailed in Appendix A. The technique was specifically employed to search for the presence of
111 any ²⁰⁴Pb (common Pb; Pb_c) because LA-ICP-MS cannot be employed due to the unresolvable
112 isobaric interference between ²⁰⁴Pb (203.9730), and ²⁰⁴Hg (203.9735). With the SIMS
113 technique there is a potential isobaric interference from the molecular species
114 [²³²Th¹⁴⁴Nd¹⁶O₂]²⁺ (mass 407.9379, M/z = 203.9690). This interference can be resolved by
115 correlating [²³²Th¹⁴⁴Nd¹⁶O₂]²⁺ counts per second (cps) with ¹⁴³Nd³¹P¹⁶O₂ (205.87) in the 5037
116 monazite sample and comparing this to Moacyr reference material data, which shows that these
117 data follow a linear correlation (more details in Appendix A). SIMS analyses reported a
118 maximum of 0.06 cps associated with ²⁰⁴Pb estimated in Moacyr reference material. As the
119 counts of mass 204 in sample 5037 monazite are less than, or overlap, those for Moacyr (2.8

120 cps and 3.7 cps respectively; Appendix C), the figure of 0.06 cps for ^{204}Pb is applied as a
121 maximum correction for common Pb on ^{206}Pb , ^{207}Pb and ^{208}Pb in sample 5037 monazite. Age
122 data from SIMS have higher uncertainties than those from LA-ICP-MS as the SIMS
123 methodology was optimized to assess Pb_c and not to obtain high-precision dates. U–Th–Pb
124 EMP dating was conducted using a CAMECA SXFive at the Microcharacterization Center
125 Raimond Castaing, at Toulouse (France). The analytical conditions were 15 keV and 200-300
126 nA, following the protocol outlined in Laurent et al. (2016), and are detailed along with age
127 reproducibility in Appendix A.

128 Nanoscale characterization by TEM and scanning transmission electron microscopy
129 (STEM) were performed with a Cs-corrected NeoARM200F Cold FEG TEM operated at 200
130 keV, owned by the Consortium Lyon Saint-Etienne de Microscopie (FED 4092) and hosted
131 within the Hubert Curien Laboratory, Saint-Etienne (France). APT data were collected using a
132 CAMECA Local Electrode Atom Probe LEAP 4000X HR hosted at the Geoscience Atom
133 Probe Facility at Curtin University, Perth (Australia). APT data were collected using a UV laser
134 ($\lambda = 355 \text{ nm}$) pulsed at 125 kHz and 30-300 pJ (details in Appendix A). In the APT mass spectra,
135 peaks at least twice higher than the background level were identified and reconstructed in 3
136 dimensions. For monazite, voltage evolution reconstructions were utilized with an evaporation
137 field of 27.02 V/nm^2 and an atomic volume of 0.01245 nm^3 (Fougerouse et al., 2021c). TEM
138 samples were prepared using a with a Thermo Fisher Scientific FEI Helios Nanolab 600i
139 focused-ion beam scanning electron microscope (FIB/SEM) hosted by MANUTECH USD
140 platform, at Hubert Curien laboratory, Saint-Etienne (France). A Tescan Lyra3 Ga^+ FIB-SEM
141 housed at Curtin University was used for preparation on needle-shaped APT specimens. More
142 details on instrument, analytical conditions and data processing are provided in Appendix A.

143 Isotopic dates from the APT data were calculated using $^{208}\text{Pb}/^{232}\text{Th}$ ratios measured on
144 $^{208}\text{Pb}^{2+}$ and $^{232}\text{ThO}^{2+}$ peaks, following the correction procedures of (Fougerouse et al., 2020;

145 see Appendix A for details). $^{207}\text{Pb}/^{206}\text{Pb}$ ratios were estimated from APT data on galena
146 inclusions using $^{207}\text{Pb}^{2+}$ and $^{206}\text{Pb}^{2+}$ peaks and following the methodology of Blum et al., (2018)
147 to correct the effect on the thermal peak of $^{206}\text{Pb}^{2+}$ on $^{207}\text{Pb}^{2+}$ peak (see Appendix A for details).

148 **3. GEOLOGICAL CONTEXT AND SAMPLE DESCRIPTION**

149 The studied monazite grains are from an Archean granulite (sample 5037; Black et al., 1984)
150 collected at Zircon Point in the Napier Complex, East Antarctica (Fig. 1A, B). The granulite is
151 a garnet-rich migmatized paragneiss preserving a well-developed, high-grade, layer-parallel
152 fabric composed of rutilated quartz (Rt-quartz) ribbons, mesoperthitic feldspar, sillimanite and
153 elongated poikiloblastic garnet (Appendix B.1, S₁, S₂; Black et al., 1983, 1984). This mineral
154 paragenesis corresponds to a major late-Archean ultrahigh temperature (UHT) event (1050 –
155 1120°C, 7-11 kbar) at *ca.* 2.58 – 2.48 Ga (Harley and Motoyoshi, 2000; Hokada et al., 2004
156 Kelly and Harley, 2005).

157 The sample is affected by retrogression involving the development of secondary biotite
158 within fractures in garnet (Appendix B.1, S₃; Black et al. 1983), exsolution of perthitic feldspar
159 and the recrystallization of the quartzo-feldspathic matrix as fine-grained granoblastic
160 aggregates containing rutile-free quartz (Appendix B.1; Black et al., 1983). This retrogressive
161 episode in the southern Napier Complex area, including Zircon Point, corresponds to
162 amphibolite-facies conditions and is associated with localized shearing and pegmatite
163 intrusions. This event overprints the Napier Complex, especially in Casey Bay and is temporally
164 constrained by ID-TIMS U–Pb zircon and monazite discordant fractions from paragneiss at
165 1073 Ma and 1087 ± 29 Ma (zircon from McIntyre Island; Black et al., 1983, monazite from
166 Zircon Point; Black et al., 1984, Fig. 1B) as well as by a Pb-total age on monazite from a
167 pegmatite at 1094 ± 67 Ma (Zircon Point; Asami et al., 2002). Hence, this lower-grade event
168 has been linked to the Rayner Structural Episode, which took place in the Rayner Complex at

169 amphibolite- to granulite-facies conditions around 1000 – 900 Ma ago (Black et al., 1987;
170 Harley and Hensen, 1990; Harley, 2003; Sheraton et al., 1980). At *ca.* 500-550 Ma,
171 hydrothermal activity is reported in the Napier Complex (Carson et al., 2002) and intrusion of
172 pegmatites in the nearby Ayatollah Island (Fig. 1B) is recorded by a Rb–Sr age on a pegmatite
173 at 522 ± 10 (2σ) Ma. These events reflect renewed magmatic and hydrothermal activity at
174 Zircon Point (Black et al., 1983).

175 Monazite grains are hosted in garnet, sillimanite, Rt-quartz or along grain boundaries in the
176 S_2 or recrystallized S_3 quartzo-feldspathic matrix. Previous petrographic and isotopic work
177 (isotope dilution thermal ionization mass spectrometry ID-TIMS on multigrain separates) on
178 monazite from sample 5037 identified three optically-distinct colour groups that were
179 correlated with the monazite host mineral and recorded three distinct, discordant isotopic
180 compositions (Fig. 1C; Black et al., 1984). The three groups define a discordant line (mean
181 square weighted deviation - MSWD = 11), with upper and lower intercepts at 2429 ± 17 (2σ)
182 Ma and 1087 ± 29 (2σ) Ma respectively (Fig. 1C). Chemical compositions were reported to be
183 similar for the three monazite groups, and TEM investigations did not show differences in
184 crystallinity (Black et al., 1984). Brown monazite, hosted either in garnet or Rt-quartz, were <
185 30% discordant whereas clear monazite (yellow and grey), hosted in the quartzo-feldspathic
186 matrix, were found to be at least 50% discordant (Fig. 1C). This unique pattern of discordance
187 was tentatively explained in term of variable Pb loss with the three groups reflecting the
188 differing capacities of their host mineral to shield the monazite crystals from late, post-
189 metamorphic fluids (Black et al., 1984).

190 **4. MONAZITE CHARACTERIZATION**

191 A microscale analytical survey of 35 *in-situ* monazite grains was complemented by
192 nanoscale characterization of a subset of these monazite crystals (Mnz2, Mnz4, Mnz17, Mnz25;

193 Fig.2, Appendix B.2) according to their textural position (host mineral). A single TEM foil was
194 prepared from a monazite grain hosted in both Rt-quartz (Mnz17; Fig. 2A) and garnet (Mnz4;
195 Appendix B.2) and three TEM foils were prepared from a monazite grain located in the quartzo-
196 feldspathic matrix (Mnz25; Fig. 2B). Fourteen needle-shaped atom probe specimens were
197 prepared from Rt-quartz hosted monazite (Mnz17; Fig. 2A) and quartzo-feldspathic matrix
198 hosted monazite (Mnz25 and Mnz2; Fig. 2B, C). Specimen locations are shown in Fig. 2A, C,
199 F.

200 **4.1. Microscale to nanoscale features**

201 Monazite crystals display complex textural features in greyscale back-scattered electron
202 (BSE) images (Fig. 2). These include a core-rim texture, highlighted generally by dark cores
203 (Fig. 2A-C), bright (Th-rich) linear features traversing the core (Fig. 2B, Appendix B.2),
204 zonation (Fig. 2A) or overgrowths (Appendix B.2). These different textures are present in
205 monazite grains from different hosts but are not systematically present in all grains. Monazite
206 located in the quartzo-feldspathic matrix are range between 50-250 μm in size while monazite
207 in garnet or Rt-quartz are range between 20-80 μm in size. Sub-micrometer ($\varnothing < 1\mu\text{m}$) dark
208 (low-BSE coefficient) circular spots are present in all monazite grains, as are sub-micrometer
209 ($\varnothing < 1 \mu\text{m}$), bright (high-BSE coefficient) circular spots (Fig. 2D-F, Appendix B.2). Bright
210 spots are larger in monazite hosted in the quartzo-feldspathic matrix than those hosted in Rt-
211 quartz or garnet (Fig. 2D-F). They are also more abundant and larger in the rim of Mnz25 than
212 in the core (Fig. 2E).

213 At the nanoscale the bright spots correspond to distinct crystalline Pb-bearing minerals
214 (lightest nanoscale features on STEM images; Fig. 3) and are often spatially associated with a
215 dark silicate and amorphous material (Fig. 3). Individual Pb-bearing minerals and amorphous
216 silicate material also exist. The distribution and the size of these Pb-bearing minerals varies

217 within the grain (e.g. core versus rim) and with the textural position of the monazite grain.
218 Monazite grains in Rt-quartz and garnet have a large number of Pb-bearing minerals ($\varnothing < 50$
219 nm; Fig. 3A, Appendix B.3) compared to grains within the quartzo-feldspathic matrix ($\varnothing > 50$
220 nm; Fig. 3B, C). In monazite grains from the quartzo-feldspathic matrix, Pb-bearing minerals
221 are also more abundant and smaller in the rim ($\varnothing < 100$ nm; Fig. 3B), than in the core ($\varnothing > 100$
222 nm; Fig. 3C).

223 Two of the largest Pb-bearing minerals ($\varnothing \sim 1 \mu\text{m}$) have been analyzed by APT. These
224 minerals comprise Pb and S, (Fig. 4) and are devoid of U or Th (Fig. 4B). Compositions
225 estimated from the APT data ($S = 47.76 \pm 0.02$ at % and $Pb = 52.18 \pm 0.02$ at % and $S = 48.79$
226 ± 0.06 at % and $Pb = 50.60 \pm 0.06$ at %; Appendix B.6) are consistent with the stoichiometry
227 of galena. Electron diffraction patterns acquired by TEM on a similar Pb-bearing mineral ($\varnothing \sim$
228 500 nm) are compatible with these minerals being galena (Appendix B.4).

229 **4.2. Isotopic data and geochronology**

230 The corrected $^{206}\text{Pb}/^{204}\text{Pb}$ ratios obtained with SIMS are on average, 44284 for sample 5037
231 monazite and 9225 for Moacyr reference material. In each case the amount of common ^{206}Pb
232 ($^{206}\text{Pb}_c$), is significantly less than 1% of total ^{206}Pb (0.038% for sample 5037 and 0.189% for
233 Moacyr). Thus, monazite crystals contain negligible ^{204}Pb indicating that Pb_c can be discounted
234 as a contaminant in the LA-ICP-MS results and as a contributor to the Pb present in the galena
235 grains.

236 The analytical volume of the different geochronological approaches applied to the monazite
237 grains range over nine orders of magnitude. Dates from LA-ICP-MS (Appendix D), SIMS
238 (Appendix C) and EMP (Appendix E) techniques range between 2435 ± 150 Ma (2σ) Ma and
239 874 ± 28 Ma (2σ) and are independent of the chosen chronometer ($^{206}\text{Pb}/^{238}\text{U}$, $^{208}\text{Pb}/^{232}\text{Th}$; Fig.
240 5, Appendix F). $^{208}\text{Pb}/^{232}\text{Th}$ dates from APT data tend towards the lower end of this spectrum,

241 whilst ID-TIMS on multiple grains (Black et al. 1984) tend towards the oldest dates (Fig. 5).
242 Moreover, at the scale of the population, the spread of monazite dates is systematically related
243 to where the monazite is hosted and not to its Th/U ratio nor to the analysis location with respect
244 to core and rim (Fig. 5, Appendix G.1-4).

245 U–Pb isotopic data gathered *in-situ* by LA-ICP-MS and SIMS are discordant and spread
246 along a discordia line, D_{all} , defined by an upper intercept of 2383 ± 36 Ma (2σ) and a lower
247 intercept of 931 ± 45 Ma (2σ) (MSWD = 4.7; Fig. 6A). U–Pb and Th–Pb systems are also
248 discordant (Appendix G.5). The data from monazite grains hosted in Rt-quartz and garnet plot
249 close to the upper intercept of the discordia line and show less than 50% Pb-loss. These data
250 alone yield an upper and a lower intercept of 2440 ± 39 Ma (2σ) and 1045 ± 132 Ma (2σ)
251 respectively (MSWD = 0.84, discordia D_{IM} ; Fig. 6A, Appendix G.6). In contrast, the monazite
252 grains hosted in the quartzo-feldspathic matrix record up to 90% Pb-loss (Fig. 6A).

253 LA-ICP-MS and SIMS U–Pb data from monazite grains hosted in the quartzo-feldspathic
254 matrix (Mnz2 and Mnz25; Fig. 3B, C) define two distinct discordia trends when ranged by
255 galena-rich rim or galena-poor core region (Fig. 6B) and also related locally to the Th/U ratio
256 of the analytical spots (Appendix G.7). The discordia D_{LI} from the galena-rich rim region
257 (yellow symbols, MSWD = 2), yields upper and lower intercepts at 2434 ± 181 Ma (2σ) and
258 1049 ± 248 Ma (2σ) respectively, and intersect the $^{207}\text{Pb}/^{206}\text{Pb}$ axis at $(^{207}\text{Pb}/^{206}\text{Pb})_{DLI} = 0.21 \pm$
259 0.03 (2σ). Data from the galena-poor core region (blue symbols) form a discordia D_{FI} (MSWD
260 = 2.6) which intersects the $^{207}\text{Pb}/^{206}\text{Pb}$ axis at $(^{207}\text{Pb}/^{206}\text{Pb})_{DFI} = 0.16 \pm 0.03$ (2σ) and has upper
261 and lower intercepts with concordia at 2120 ± 207 Ma (2σ) and 631 ± 224 Ma (2σ) respectively.
262 By fixing the upper intercept at 2440 Ma for the sparse galena domain data, the lower intercept
263 is at 861 ± 58 Ma (2σ) (discordia D_{fix} , MSWD = 4).

264 APT-derived $^{208}\text{Pb}/^{232}\text{Th}$ dates from monazite grains hosted in the quartzo-feldspathic
265 matrix (Mnz25 and Mnz2) and the Rt-quartz (Mnz17) are calculated from areas that do not

266 contain galena (Fig. 7, Appendix H, APT mass spectrum Appendix B.5). $^{208}\text{Pb}/^{232}\text{Th}$ dates range
267 between 1188 ± 202 Ma (2σ) and 712 ± 121 Ma (2σ) (Fig. 5, Appendix G.8) and statistically
268 correspond to a single date population (MSWD = 0.72; Appendix G.8-9). Using the complete
269 dataset, the mean $^{208}\text{Pb}/^{232}\text{Th}$ ratio is 0.0518 ± 0.0137 (2σ) corresponding to a date of $1021 \pm$
270 263 Ma (2σ). The $^{208}\text{Pb}/^{232}\text{Th}$ mean for specimens obtained from the rim of Mnz25 and Mnz2
271 is 0.0540 ± 0.0107 (2σ) yielding a date of 1063 ± 205 Ma (2σ) (MSWD = 0.34) while the mean
272 $^{208}\text{Pb}/^{232}\text{Th}$ for core specimens from the same grains is 0.0497 ± 0.0156 (2σ) corresponding to
273 979 ± 301 Ma (2σ) (MSWD = 1.04; Appendix G.8).

274 APT-derived $^{207}\text{Pb}/^{206}\text{Pb}$ ratios from the two analysed galena (Gn 1 and Gn 2; Fig. 4) are
275 0.20 ± 0.02 (1σ) and 0.150 ± 0.003 (1σ) respectively. The APT data show no peaks associated
276 with ^{204}Pb (Fig. 4C).

277 **5. DISCUSSION**

278 **5.1. Interpretation of microscale age pattern**

279 Isotopic analyses of Pb by SIMS in selected grains did not show any ^{204}Pb component in
280 the time resolved signal, which is interpreted as the absence of significant “common”-Pb in the
281 microscale analyses. Consequently, all the Pb present in monazite and galena is interpreted to
282 be of radiogenic origin and is derived from within the monazite.

283 Considering the whole dataset ($n = 89$), the discordia D_{all} MSWD (4.7) indicates that the
284 dispersion of the data cannot result from a single population (i.e. a single disturbing event) at
285 95% confidence level (Wendt and Carl, 1991). In contrast, the D_{M} discordia derived from
286 monazite hosted in Rt-quartz and garnet yields an acceptable MSWD of 0.84 compatible with
287 a single disturbing event and is thus the most robust to derive monazite crystallization age (t_0)
288 at 2440 ± 39 Ma (Fig. 6A). This age is identical within errors to previous upper intercept ages
289 calculated with ID-TIMS data on monazite and zircon grains from Casey Bay (Fig. 1C; Black

290 et al., 1984, 1983) and to 2451 ± 15 Ma zircons in equilibrium with garnet from Crosby
291 Nunataks in Amundsen Bay (Fig. 1A; Taylor et al., 2017). Even if *in-situ* isotopic dating on
292 zircon may present slightly older ages than obtained in monazite (e.g. Hokada et al., 2004; Kelly
293 and Harley, 2005), monazite are truly and fully included in garnet implying garnet growth
294 and/or recrystallization through to that age, extending the timescale of the UHT to HT
295 metamorphism even further. Thus, the monazite age of 2440 ± 39 Ma provides a lower limit
296 for the UHT metamorphism in this part of the Napier Complex. The lower intercept t_1 of the
297 D_{IM} discordia (1045 ± 132 Ma) is within error of the Rayner Complex event and reflects the
298 time of U–Th–Pb chronometer disturbance. This is confirmed by the $^{208}\text{Pb}/^{232}\text{Th}$ average age
299 of 1021 ± 263 Ma (2σ) derived by APT analysis of galena-free monazite that points to a
300 complete resetting of the monazite matrix during the Rayner Complex tectonothermal event.

301 The monazite grains (Mnz25 and Mnz2) hosted in the quartzo-feldspathic matrix show two
302 discordia trends (yellow and blue symbols, Fig. 6B). D_{LI} discordia is defined by the galena-rich
303 rim and is consistent with the D_{IM} discordia. D_{FI} is defined by the galena-poor core,
304 corresponding to areas which have undergone 70 – 90 % Pb^* loss at t_1 , and suggests a younger
305 disturbing event, defined by the lower intercept at $t_2 = 631 \pm 224$ Ma (2σ) (Fig. 6B). This age
306 lies within uncertainty of the timing of pegmatite intrusions within the Napier Complex at Casey
307 Bay at *ca.* 530 Ma (Carson et al., 2002; Black et al., 1983), so may correspond with this
308 hydrothermal activity (t_2).

309 **5.2. Origin of discordance revealed at nanoscale**

310 Black et al. (1984) highlighted that the least discordant monazite fraction was brown in
311 color, whereas the most discordant was clear (grey and yellow). Our microscale data confirm a
312 similar systematic relationship between monazite color and the percentage of Pb-loss. In
313 addition, SEM and TEM investigations revealed that the color relates to the density of galena

314 inclusions, with monazite showing the highest density of galena being brown in color, whilst
315 the clearest monazite grains contain a lower density of galena inclusions (Fig. 3, 5, 6).

316 Considering the microscale U–Th–Pb data, the dates of monazite hosted in the quartzo-
317 feldspathic matrix, tend toward the lower intercept t_1 (80 % Pb-loss ; Fig. 5) whereas the dates
318 from monazite hosted in Rt-quartz and garnet tend toward the upper intercept (t_0) implying only
319 limited Pb* loss (10-50 %) at the grain scale . This difference is again explained by the large
320 amount of galena, homogeneously distributed considering a micrometric analytical volume, in
321 Rt-quartz hosted monazite compared to monazite hosted in the quartzo-feldspathic matrix (Fig.
322 3A) Thus, the discordia (D_M) is interpreted as a mixing pattern between galena and monazite
323 host, representing two different reservoirs of Pb* derived from the monazite itself. A similar
324 pattern is observed within individual grains (e.g. Mnz25), where core regions with a smaller
325 number of galena show a higher percentage of Pb-loss than the galena-rich rim (Fig. 6B).

326 The ability of monazite to retain galena crystals and thereby much of the Pb* is partly related
327 to their textural position; monazite crystals hosted in Rt-quartz and garnet retain more Pb* in
328 the form of galena than monazite crystals hosted in the quartzo-feldspathic matrix (Fig. 3, 5,
329 6A). High retention of Pb* is associated with a small galena size (< 50 nm), and a more
330 homogenous distribution through the crystal (Fig. 3). This property could be related to fluids
331 access to monazite. Rt-quartz and garnet, which are anhydrous UHT phases, could limit the
332 quantity of fluids which are thus rapidly saturated in Pb, inducing a short-range (re)precipitation
333 of Pb-bearing nanominerals within the grain. In contrast, a larger quantity of fluids might access
334 monazite hosted in quartzo-feldspathic matrix implying a more efficient leaching of Pb* which
335 is then lost from the grain. Shielding of monazite by its host-mineral, also observed at other
336 UHT localities (e.g. Paquette et al., 2004; Madagascar), does not act as the trigger for the
337 development of the Pb-bearing minerals within monazite but is instrumental to their preferential

338 preservation and retention. Further studies will be undertaken to characterize the mineralogical
339 variety of the Pb-bearing nanominerals present in monazite grains.

340 To summarize, the difference in color is interpreted to relate to the amount and distribution
341 of galena crystals within the different monazite grains, which in turn is related to the percentage
342 of Pb-loss. The inverse correlation between the percentage of Pb-loss and the amount of galena
343 (Fig. 3, 5, 6) reflects partial retention of radiogenic Pb^* at the grain scale through the
344 crystallization of galena. The volume analyzed with micro-scale dating methods (ID-TIMS,
345 LA-ICP-MS, SIMS and EMP) therefore corresponds to a mixing between monazite and galena
346 preserving distinct isotopic composition. The retention of galena is promoted by monazite
347 shielding in (anhydrous) UHT phases like garnet and Rt-quartz.

348 The largest Pb-bearing nanominerals observed in this study have been identified as galena
349 (PbS). Crystallization of galena requires Pb but also S which may be derived either from an
350 external source such as metamorphic fluids or from the monazite itself. Sulphur incorporation
351 in the monazite lattice occurs mostly through the clino-anhydrite substitution $Ca^{2+} + S^{6+} =$
352 $REE^{3+} + P^{5+}$ (Chakhmouradian and Mitchell, 1999), although other studies suggest more
353 complex substitutions involving S^{2-} and S^{4+} (Broom-Fendley et al., 2020). The presence of S-
354 rich monazite in metamorphic rocks is well-documented, including in UHT granulite (Laurent
355 et al., 2016). Under low-grade metamorphic conditions (greenschist facies), S incorporation in
356 monazite is typically associated with high common Pb content and ore precipitation in the host
357 rock (Krenn et al., 2011; Pršek et al., 2010; Suzuki and Kato, 2008). Under high-grade
358 conditions, S-rich monazite reflects Fe-sulphide breakdown under oxidizing conditions and
359 have been reported to contain negligible common Pb (Laurent et al., 2016). Since common Pb
360 is negligible in monazite and galena from the present study, sulfur could be derived from the
361 monazite itself rather than from an external source. The presence of sulfur in high-grade
362 monazite could thus contribute heavily to the preservation of Pb^* as galena nanocrystals.

363 5.3. Galena Pb isotopic signatures

364 Historically, discordance issues have been resolved by lowering the analytical volume until
365 homogenous Pb* isotope reservoirs can be analyzed separately (i.e. galena and monazite
366 matrix). As there is no U or Th in the galena, their measured $^{207}\text{Pb}/^{206}\text{Pb}$ ratios have not evolved
367 since their growth. As SIMS results support that common-Pb contamination of the monazite is
368 negligible, the $^{207}\text{Pb}/^{206}\text{Pb}$ ratio of the galena records the Pb* composition of the monazite when
369 the galena crystallised. Since the monazite crystallisation age is known, then the $^{207}\text{Pb}/^{206}\text{Pb}$ of
370 galena can be used to estimate the time of Pb* isolation from U and Th in the host monazite,
371 which corresponds to the time of galena growth. The evolution of the Pb isotopic ratio of the
372 monazite is constrained by the geological history highlighted in the previous sections and thus
373 bounded by the *ca.* 2440 Ma (t_0), 1045 Ma (t_1), and 550 Ma (t_2) geological events (Fig. 8C).
374 This assumption is confirmed by the scatter of microbeam analyses that fall in a triangle
375 bounded by *ca.* 2.44 Ga, 1.05 Ga and 0.55 Ga in the Tera-Wasserburg plot (Fig. 6).

376 The $^{207}\text{Pb}/^{206}\text{Pb}$ ratio measured in Gn 1 is best explained by Pb* isolation at 1045 Ma from
377 a monazite that crystallized at 2440 Ma, which would correspond to a theoretical $^{207}\text{Pb}/^{206}\text{Pb}$ of
378 0.2108 identical within uncertainty to the measured ratio of 0.20 ± 0.02 (1σ) in Gn 1 (Fig. 8A,
379 C). The isolation time of Pb₁* (i.e. Pb* formed by radioactive decay within monazite between
380 2440 and 1045 Ma) at *ca.* 1045 Ma is supported by the $^{208}\text{Pb}/^{232}\text{Th}$ date of 1171 ± 170 Ma
381 (Appendix G.8) obtained by APT from the host monazite adjacent to Gn 1 in specimen M6
382 (Fig. 4A). Thus, we interpret that the isolation of Pb₁* and the crystallization of galena Gn 1
383 occurred at $t_1 = 1045$ Ma.

384 Galena Gn 2 has a significantly different $^{207}\text{Pb}/^{206}\text{Pb}$ ratio of 0.150 ± 0.003 (1σ) that cannot
385 be explained by a single Pb* isolation event since the present-day $^{207}\text{Pb}/^{206}\text{Pb}$ ratio of a monazite
386 that crystallized at 2440 Ma would be 0.1585 (Fig. 8A). The possibility for Gn 2 to result from

387 a mixing of two Pb^* components is thus explored using the well-known t_0 , t_1 and t_2 events. This
388 scenario involves a first Pb^* component (Pb_1^*) produced by U and Th decay between t_0 and t_1
389 with a theoretical $^{207}Pb/^{206}Pb$ isotopic signature of 0.2108, and a second Pb^* component (Pb_2^*)
390 produced by U and Th decay between t_1 and t_2 with a theoretical $^{207}Pb/^{206}Pb$ isotopic signature
391 of 0.0901. At 550 Ma, the $^{207}Pb/^{206}Pb$ ratio of 0.150 recorded by Gn 2 is then obtained by a
392 mixture of 53% Pb_2^* and 47% Pb_1^* , in a grain which underwent 70% Pb_1^* loss at t_1 with 30%
393 remaining captured by the galena (Fig. 8B, C). This 70% Pb_1^* loss fits the microscale U–Th–
394 Pb data for monazite grain 25 domains with a low density of inclusions (Fig. 6B). The
395 $^{208}Pb/^{232}Th$ date of 712 ± 121 Ma (2σ) (Appendix G.8) obtained by APT from the host monazite
396 adjacent to Gn 2 in specimen M17 (Fig. 4A) supports the formation of Gn 2 at t_2 , a younger
397 event than t_1 . This preferred scenario is not unique since: (1) microscale data suggests variable
398 Pb_1^* loss at t_1 , ranging from 10 to 90 % (Fig. 6) and (2) variable proportions of Pb_1^* and Pb_2^*
399 could be mobilized and mixed at t_2 , corresponding to a theoretical range of $^{207}Pb/^{206}Pb$ isotopic
400 compositions between 0.0901 – 0.1806 for the galena (Fig. 8C). This observation cautions about
401 the interpretation of $^{207}Pb/^{206}Pb$ ratios in Pb-rich nanominerals in term of ages.

402 **5.4. Time-integrated model of monazite evolution**

403 The theoretical evolution of U–Pb and Pb–Pb ratios in a monazite that crystallized at *ca.*
404 2440 Ma have been modelled and the results are displayed in Tera-Wasserburg diagrams along
405 with snapshots of Pb distribution in the monazite crystal over time (Fig. 8D). After monazite
406 crystallization at t_0 , U and Th decay in monazite produce Pb_1^* (red spots, Fig. 8D). The APT
407 average $^{208}Pb/^{232}Th$ age of 1021 ± 263 Ma (2σ) indicates that the monazite matrix becomes
408 completely reset at the nanoscale. This resetting event corresponds to the amphibolite-facies
409 Rayner event at *ca.* 1045 Ma. This metamorphic event is recorded in our rock sample 5037 by
410 garnet retrogression into biotite and by recrystallization of (UHT) Rt-quartz in rutile-free, low-
411 Ti quartz ribbons. Clear evidence of fluid-rock interaction and plastic deformation thus exists

412 in the rock sample 5037 at *ca.* 1045 Ma. Lead mobility in monazite has been shown to be
413 enhanced both by fluid present conditions (Seydoux-Guillaume et al., 2002) and deformation
414 (Erickson et al., 2015; Fougereuse et al., 2021b) or a combination of both (Wawrzenitz et al.,
415 2012).

416 In presence of reactive metamorphic fluids, experimental studies demonstrate that the
417 resetting of monazite U–Pb and Th–Pb chronometers at the nanoscale could arise through
418 pseudomorphic replacement with the formation of a new monazite free of Pb* only recognizable
419 at the nanoscale (Grand’Homme et al., 2018, 2016). Whilst the APT age of 1021 ± 263 Ma (2σ)
420 suggests that the monazite matrix is completely reset at t_1 , we cannot completely exclude that
421 subordinate nanodomains of monazite crystallized at 2440 Ma may still be present after t_1 ,
422 accounting for the dispersion and large uncertainties of the monazite matrix dates measured by
423 APT (Appendix G.9). Compared to these experimental studies, the replacement process in this
424 natural example is coupled with Pb-bearing nanominerals (galena) crystallization. This contrast
425 could reflect differences in experimental versus natural rock reaction kinetics or fluid/mineral
426 ratios, or fluid compositions. Indeed, nanopores filled with SiO₂ are frequently observed in
427 experimental studies because a NaOH fluid saturated in Si is used. In natural monazite, the local
428 fluid saturation in Pb might be achieved by relatively low fluid/monazite ratio typical of dry
429 rocks like UHT granulite and a high Pb* concentration typical of old Th-rich monazite.

430 Following the t_1 event, Pb₂* forms from the further decay of U and Th in the monazite (green
431 spots, Fig. 8D). At *ca.* 550 Ma (t_2), a hydrothermal event associated with pegmatite formation
432 triggers the crystallization of a second generation of galena (Gn 2) composed by the mixing of
433 Pb₁* + Pb₂*. The Pb₂* component is derived from the monazite matrix at t_2 and correspond to
434 Pb* growth between t_1 and t_2 . Mobilization of Pb₂* to form Gn 2 is more cryptic as it is not
435 related to an extensive resetting of the Th–Pb chronometer in the monazite matrix compared to
436 the first generation of galena. The monazite matrix adjacent to Gn 2 yields the youngest Th–Pb

437 date of 712 ± 121 Ma (2σ), which sits between t_1 and t_2 . Consequently, Pb migration at t_2
438 occurred at a smaller scale than at t_1 and might not be completely resolved at the current scale
439 of investigation. This is confirmed by the microscale observation that in contrast to t_1 event, the
440 effect of the t_2 event is insufficient to cause significant Pb^* loss at the grain scale (Fig. 6). The
441 galena 2 therefore rather witnesses intra-grain and short-range redistribution of Pb, involving a
442 Pb_2^* and a Pb_1^* component that could be derived from either the first galena (Gn 1) or from
443 monazite matrix in case of old nanodomains have been preserved in the matrix at t_1 .

444 **6. CONCLUSION and PERSPECTIVES**

445 This study explores the isotopic disturbance of the U–Th–Pb systems in monazite from a
446 UHT Archean granulite using multiple methods for characterization and dating from the micro-
447 (LA-ICP-MS, SIMS, EMP) to the nanoscale (TEM, APT). At the microscale the dates are
448 discordant and spread along a discordia between *ca.* 2440 and *ca.* 1045 Ma. Our observations
449 reveal that the least discordant monazite grains are brown in color because they contain a high
450 density of small (~ 50 nm) Pb-bearing nanominerals homogeneously distributed in the grain
451 whereas the most discordant and optically clear monazite grains contain larger (50- 500 nm)
452 but sparser Pb-bearing nanominerals, some of them being identified as galena (PbS) on the basis
453 of TEM and APT observations. The discordia observed with conventional *in-situ* methods at
454 the microscale thus reflects a mixing within the analytical volume of matrix monazite and
455 galena. The percentage of Pb-loss is in turn linked to monazite textural position as initially
456 observed by Black et al. (1984). Monazite shielded in UHT phases like garnet or Rt-quartz
457 show a low percentage of Pb-loss and a high density of galena inclusions. In contrast monazite
458 hosted in the re-equilibrated quartzo-feldspathic matrix show a high percentage of Pb-loss and
459 lower density of galena inclusions. The retention of Pb^* in galena is promoted by monazite
460 shielding in (anhydrous) UHT phases like garnet and Rt-quartz.

461 The Pb isotopic compositions of the galena grains are variable but imply an *in-situ*
462 radiogenic origin with no participation of common Pb. The $^{207}\text{Pb}/^{206}\text{Pb}$ ratios of the galena,
463 when considered in combination with the $^{208}\text{Pb}/^{232}\text{Th}$ ages of the monazite matrix (excluding
464 galena) measured with APT, and the constrains given by regional geology, indicate two
465 episodes of Pb^* mobility. This study suggests that monazite crystallized at *ca.* 2440 Ma and was
466 affected at *ca.* 1045 Ma by variable Pb^* -loss at the grain scale, characterized at the nanoscale
467 by a resetting of the monazite matrix through pseudomorphic replacement associated with Pb^*
468 retention as galena Gn 1 in variable proportions. A second episode of Pb^* mobility is recorded
469 by the crystallization of a second generation of galena Gn 2 and is likely related to a younger
470 event at *ca.* 550 Ma. Pb^* in Gn 2 galena corresponds to a mixing of Pb_1^* and Pb_2^* likely
471 reworked from the pre-existing Gn 1 (Pb_1^*) and monazite matrix (Pb_2^*) with much more
472 localized effect on the resetting of the monazite matrix as no date of 550 Ma was found by APT.

473 Combining a multi-scale characterization, this study demonstrates the importance of
474 nanoscale structural, chemical and isotopic observations to understand microscale age
475 disturbances by providing a new perspective on the origin of the discordance in monazite.
476 Indeed, the retention of Pb^* in the form of Pb-bearing nanominerals within monazite grain could
477 be a phenomenon that is, if not prevalent, at least shared by monazite crystals when certain
478 conditions are met. These conditions may include an ancient and long-lived geological history
479 (Archean – Proterozoic) resulting in high Pb^* content, a monazite composition having a
480 sufficient S content to form galena and the presence of reactive fluids. However other Pb-
481 bearing nanominerals might crystallize if S is unavailable. For example, Pb-bearing
482 nanominerals have been found in discordant Archean UHT monazite from Madagascar
483 (Paquette et al., 2004; Seydoux-Guillaume et al., 2003). Hence, discordance in monazite is
484 explained by the partial loss of Pb^* through a coupled dissolution-precipitation process and the
485 retention of the remaining Pb^* within monazite as Pb^* -bearing nanominerals (e.g. galena). In

486 combination with a good understanding of the regional framework and the thermal events in an
487 area, the identification of Pb^{*}-bearing nanominerals can be used to understand the complexities
488 of Pb^{*} migration processes in minerals. The presence of numerous Pb^{*}-bearing nanominerals
489 within monazite grains therefore presents new opportunities for geochronologists to decipher
490 the thermal history of complex metamorphic terrains.

491 **Acknowledgments**

492 We thank Ph. De Parseval and S. Gouy for their technical assistance with the microprobe, C.
493 Talavera-Rodriguez for the SIMS, C. Fellah for SEM, V. Bosse and R. Dubost for the LA-ICP-
494 MS. UJM and CNRS (INSU TelluS-SYSTER and IEA nanomobility) are thanked for financial
495 support and CAMECA for access to Ivas software. D. Fougerouse acknowledges funding from
496 the Australian Research Council (DE190101307). We thank Alex Webb for editorial handling
497 and Monika Kusiak and one anonymous reviewer for providing constructive comments.

498 **Appendices**

499 Appendix A. Details on the methods, including sample preparation, analytical conditions,
500 calibration and data processing

501 Appendix B. Complementary observations of microscale to nanoscale features including
502 optical microscopy, scanning electron imaging, transmission electron microscopy and atom
503 probe mass spectrum of monazite

504 Appendix C. U-Th-Pb SIMS dataset

505 Appendix D. U-Th-Pb LA-ICP-MS dataset

506 Appendix E. U-Th-Pb EMP dataset

507 Appendix F. U-Th-Pb data plotted on figure 5

508 Appendix G. Complementary figures of U–Th–Pb geochronology

509 Appendix H. Th-Pb APT dataset

510 **References**

511 Allègre, C.J., Albarède, F., Grünenfelder, M., Köppel, V., 1974. $^{238}\text{U}/^{206}\text{Pb}$ - $^{235}\text{U}/^{207}\text{Pb}$ -
512 $^{232}\text{Th}/^{208}\text{Pb}$ Zircon Geochronology in Alpine and Non-Alpine Environment.

513 *Contributions to Mineralogy and Petrology* 43, 194.

514 Arcuri, G.A., Moser, D.E., Reinhard, D.A., Langelier, B., Larson, D.J., 2020. Impact-

515 triggered nanoscale Pb clustering and Pb loss domains in Archean zircon. *Contributions*

516 *to Mineralogy and Petrology* 175, 1–13. <https://doi.org/10.1007/s00410-020-01698-w>

517 Asami, M., Suzuki, K., Grew, E.S., 2002. Chemical Th-U-total Pb dating by electron

518 microprobe analysis of monazite, xenotime and zircon from the Archean Napier

519 complex, East Antarctica: Evidence for ultra-high-temperature metamorphism at 2400

520 Ma. *Precambrian Research* 114, 249–275. <https://doi.org/10.1016/S0301->

521 [9268\(01\)00228-5](https://doi.org/10.1016/S0301-9268(01)00228-5)

522 Black, L.P., Fitzgerald, J.D., Harley, S.L., 1984. Pb isotopic composition, colour, and

523 microstructure of monazites from a polymetamorphic rock in Antarctica. *Contributions*

524 *to Mineralogy and Petrology* 85, 141–148.

525 Black, L.P., Harley, S.L., Sun, S.S., McCulloch, M.T., 1987. The Rayner Complex of East

526 Antarctica: complex isotopic systematics within a Proterozoic mobile belt. *Journal of*

527 *Metamorphic Geology* 5, 1–26. <https://doi.org/10.1111/j.1525-1314.1987.tb00366.x>

528 Black, L.P., James, P.R., Harley, S.L., 1983. Geochronology and geological evolution of

529 metamorphic rocks in the Field Islands area, East Antarctica. *Journal of Metamorphic*

530 *Geology* 1, 277–303. <https://doi.org/10.1111/j.1525-1314.1983.tb00276.x>

531 Blum, T.B., Reinhard, D.A., Chen, Y., Prosa, T.J., Larson, D.J., Valley, J.W., 2018.
532 Uncertainty and sensitivity analysis for spatial and spectral processing of Pb isotopes in
533 zircon by atom probe tomography. *Geophysical Monograph Series* 232, 327–350.
534 <https://doi.org/10.1002/9781119227250.ch16>

535 Broom-Fendley, S., Smith, M.P., Andrade, M.B., Ray, S., Banks, D.A., Loye, E., Atencio, D.,
536 Pickles, J.R., Wall, F., 2020. Sulfur-bearing monazite-(Ce) from the Eureka carbonatite,
537 Namibia: oxidation state, substitution mechanism, and formation conditions.
538 *Mineralogical Magazine* 84, 35–48. <https://doi.org/10.1180/mgm.2019.79>

539 Cappelli, C., Pérez-Huerta, A., 2020. Effect of crystallographic orientation on atom probe
540 tomography geochemical data? *Micron* 137, 102910.
541 <https://doi.org/10.1016/j.micron.2020.102910>

542 Carson, C.J., Ague, J.J., Grove, M., Coath, C.D., Harrison, T.M., 2002. U-Pb isotopic
543 behaviour of zircon during upper-amphibolite facies fluid infiltration in the Napier
544 Complex, East Antarctica. *Earth and Planetary Science Letters* 199, 287–310.
545 [https://doi.org/10.1016/S0012-821X\(02\)00565-4](https://doi.org/10.1016/S0012-821X(02)00565-4)

546 Chakhmouradian, A.R., Mitchell, R.H., 1999. Niobian ilmenite, hydroxylapatite and sulfatian
547 alternative hosts for incompatible in calcite elements. *Canadian Mineralogist* 37, 1177–
548 1189.

549 Corfu, F., 2013. A century of U-pb geochronology: The long quest towards concordance.
550 *Bulletin of the Geological Society of America* 125, 33–47.
551 <https://doi.org/10.1130/B30698.1>

552 Erickson, T.M., Pearce, M.A., Taylor, R.J.M., Timms, N.E., Clark, C., Reddy, S.M., Buick,
553 I.S., 2015. Deformed monazite yields high-temperature tectonic ages. *Geology* 43, 383–
554 386. <https://doi.org/10.1130/G36533.1>

555 Fougrouse, D., Cavosie, A.J., Erickson, T., Reddy, S.M., Cox, M.A., Saxey, D.W., Rickard,
556 W.D.A., Wingate, M.T.D., 2021a. A new method for dating impact events – Thermal
557 dependency on nanoscale Pb mobility in monazite shock twins. *Geochimica et*
558 *Cosmochimica Acta* 314, 381–396. <https://doi.org/10.1016/j.gca.2021.08.025>

559 Fougrouse, D., Kirkland, C., Saxey, D., Seydoux-Guillaume, A.M., Rowles, M.R., Rickard,
560 W.D.A., Reddy, S.M., 2020. Nanoscale isotopic dating of monazite. *Geostandards and*
561 *Geoanalytical Research* in press. <https://doi.org/10.1111/ggr.12340>

562 Fougrouse, D., Reddy, S.M., Saxey, D.W., Erickson, T., Kirkland, C.L., Rickard, W.D.A.,
563 Seydoux-Guillaume, A.M., Clark, C., Buick, I.S., 2018. Nanoscale distribution of Pb in
564 monazite revealed by atom probe microscopy. *Chemical Geology* 479, 251–258.
565 <https://doi.org/10.1016/j.chemgeo.2018.01.020>

566 Fougrouse, D., Reddy, S.M., Seydoux-Guillaume, A., Kirkland, C.L., Erickson, T.M.,
567 Saxey, D.W., Rickard, W.D.A., Jacob, D., Clark, C., 2021b. Mechanical twinning of
568 monazite expels radiogenic lead. *Geology* 49, 417–421.
569 <https://doi.org/https://doi.org/10.1130/G48400.1>

570 Fougrouse, D., Saxey, D., Rickard, W., Reddy, S., Verberne, R., 2021c. Standardizing
571 Spatial Reconstruction Parameters for the Atom Probe Analysis of Common Minerals.
572 *Microscopy and Microanalysis* 1–10. <https://doi.org/10.1017/S1431927621013714>

573 Gebauer, D., Grünenfelder, M., 1979. U-Th-Pb Dating of Minerals, in: Jäger, E., Hunziker,
574 J.C. (Eds.), *Lectures in Isotopic Geology*. Berlin Heidelberg New York, pp. 105–131.
575 <https://doi.org/10.1007/978-3-642-67161-6>

576 Grand’Homme, A., Janots, E., Seydoux-Guillaume, A.M., Guillaume, D., Bosse, V., Magnin,
577 V., 2016. Partial resetting of the U-Th-Pb systems in experimentally altered monazite:
578 Nanoscale evidence of incomplete replacement. *Geology* 44, 4–7.

579 <https://doi.org/10.1130/G37770.1>

580 Grand'Homme, A., Janots, E., Seydoux-Guillaume, A.M., Guillaume, D., Magnin, V.,
581 Hövelmann, J., Höschen, C., Boiron, M.C., 2018. Mass transport and fractionation
582 during monazite alteration by anisotropic replacement. *Chemical Geology* 484, 51–68.
583 <https://doi.org/10.1016/j.chemgeo.2017.10.008>

584 Harley, L., Hensen, B.J., 1990. Archean and Proterozoic high grade terranes of East
585 Antarctica (40-80°E): a case study of diversity in granulite facies metamorphism. In:
586 Ashworth, J. R. & Brown, M. (eds) *High-temperature Metamorphism and Crustal*
587 *Anatexis*. Unwin Hyman, London, 320-370

588 Harley, S.L., 2003. Archaean-Cambrian crustal development of East Antarctica: metamorphic
589 characteristics and tectonic implications. Geological Society, London, Special
590 Publications 206, 203–230. <https://doi.org/10.1144/gsl.sp.2003.206.01.11>

591 Harley, S.L., Kelly, N.M., Kusiak, M.A., 2019. Ancient Antarctica : The Archean of the East
592 Antarctic Shield. *Earth's Oldest Rocks* 865–897.

593 Harley, S.L., Motoyoshi, Y., 2000. Al zoning in orthopyroxene in a sapphirine quartzite:
594 Evidence for >1120 °C UHT metamorphism in the Napier Complex, Antarctica, and
595 implications for the entropy of sapphirine. *Contributions to Mineralogy and Petrology*
596 138, 293–307. <https://doi.org/10.1007/s004100050564>

597 Hokada, T., Misawa, K., Yokoyama, K., Shiraishi, K., Yamaguchi, A., 2004. SHRIMP and
598 electron microprobe chronology of UHT metamorphism in the Napier Complex, East
599 Antarctica: Implications for zircon growth at >1,000 °C. *Contributions to Mineralogy*
600 *and Petrology* 147, 1–20. <https://doi.org/10.1007/s00410-003-0550-2>

601 Kelly, N.M., Harley, S.L., 2005. An integrated microtextural and chemical approach to zircon

602 geochronology: Refining the Archaean history of the Napier Complex, east Antarctica.
603 Contributions to Mineralogy and Petrology 149, 57–84. <https://doi.org/10.1007/s00410->
604 004-0635-6

605 Krenn, E., Putz, H., Finger, F., Paar, W.H., 2011. Sulfur-rich monazite with high common Pb
606 in ore-bearing schists from the Schellgaden mining district (Tauern Window, Eastern
607 Alps). Mineralogy and Petrology 102, 51–62. <https://doi.org/10.1007/s00710-011-0170->
608 x

609 Kusiak, M.A., Dunkley, D.J., Wirth, R., Whitehouse, M.J., Wilde, S.A., Marquardt, K., 2015.
610 Metallic lead nanospheres discovered in ancient zircons. Proceedings of the National
611 Academy of Sciences 112, 4958–4963. <https://doi.org/10.1073/pnas.1415264112>

612 Kusiak, M.A., Kovaleva, E., Wirth, R., Klötzli, U., Dunkley, D.J., Yi, K., Lee, S., 2019. Lead
613 oxide nanospheres in seismically deformed zircon grains. Geochimica et Cosmochimica
614 Acta. <https://doi.org/10.1016/j.gca.2019.07.026>

615 Laurent, A.T., Seydoux-Guillaume, A.M., Duchene, S., Bingen, B., Bosse, V., Datas, L.,
616 2016. Sulphate incorporation in monazite lattice and dating the cycle of sulphur in
617 metamorphic belts. Contributions to Mineralogy and Petrology 171.
618 <https://doi.org/10.1007/s00410-016-1301-5>

619 Paquette, J.L., Goncalves, P., Devouard, B., Nicollet, C., 2004. Micro-drilling ID-TIMS U-Pb
620 dating of single monazites: A new method to unravel complex poly-metamorphic
621 evolutions. Application to the UHT granulites of Andriamena (North-Central
622 Madagascar). Contributions to Mineralogy and Petrology 147, 110–122.
623 <https://doi.org/10.1007/s00410-003-0549-8>

624 Peterman, E.M., Reddy, S.M., Saxey, D.W., Fougereuse, D., Quadir, M.Z., Jercinovic, M.J.,
625 2021. Trace-element segregation to dislocation loops in experimentally heated zircon.

626 American Mineralogist 106, 1971–1979. <https://doi.org/10.2138/am-2021-7654>

627 Peterman, E.M., Reddy, S.M., Saxey, D.W., Snoeyenbos, D.R., Rickard, W.D.A.,
628 Fougereuse, D., Kylander-Clark, A.R.C., 2016. Nanogeochronology of discordant zircon
629 measured by atom probe microscopy of Pb-enriched dislocation loops. *Science Advances*
630 2. <https://doi.org/10.1126/sciadv.1601318>

631 Pršek, J., Ondrejka, M., Bačík, P., Budzyń, B., Uher, P., 2010. Metamorphic-hydrothermal ree
632 minerals in the Bacúch magnetite deposit, western carpathians, Slovakia: (Sr,S)-Rich
633 monazite-(Ce) and Nd-dominant hingganite. *Canadian Mineralogist* 48, 81–94.
634 <https://doi.org/10.3749/canmin.48.1.81>

635 Seydoux-Guillaume, A.M., Fougereuse, D., Laurent, A.T., Gardés, E., Reddy, S.M., Saxey,
636 D.W., 2019. Nanoscale resetting of the Th/Pb system in an isotopically-closed monazite
637 grain: A combined atom probe and transmission electron microscopy study. *Geoscience*
638 *Frontiers*. <https://doi.org/10.1016/j.gsf.2018.09.004>

639 Seydoux-Guillaume, A.M., Goncalves, P., Wirth, R., Deutsch, A., 2003. Transmission
640 electron microscope study of polyphase and discordant monazites: Site-specific
641 specimen preparation using the focused ion beam technique. *Geology* 31, 973–976.
642 <https://doi.org/10.1130/G19582.1>

643 Seydoux-Guillaume, A.M., Paquette, J.L., Wiedenbeck, M., Montel, J.M., Heinrich, W.,
644 2002. Experimental resetting of the U-Th-Pb systems in monazite. *Chemical Geology*
645 191, 165–181. [https://doi.org/10.1016/S0009-2541\(02\)00155-9](https://doi.org/10.1016/S0009-2541(02)00155-9)

646 Seydoux-Guillaume, A.M., Bingen, B., Bosse, V., Janots, E., Laurent, A.T., 2018a.
647 Transmission Electron Microscope Imaging Sharpens Geochronological Interpretation of
648 Zircon and Monazite. *Microstructural Geochronology* 1360, 1357–1360.

649 Seydoux-Guillaume, A.M., Deschanel, X., Baumier, C., Neumeier, S., Weber, W.J., Peugot,
650 S., 2018b. Why natural monazite never becomes amorphous: Experimental evidence for
651 alpha self-healing. *American Mineralogist: Journal of Earth and Planetary Materials*,
652 103(5), 824-827.

653 Suzuki, K., Kato, T., 2008. CHIME dating of monazite, xenotime, zircon and polycrase:
654 Protocol, pitfalls and chemical criterion of possibly discordant age data. *Gondwana*
655 *Research* 14, 569–586. <https://doi.org/10.1016/j.gr.2008.01.005>

656 Taylor, R.J.M., Clark, C., Harley, S.L., Kylander-Clark, A.R.C., Hacker, B.R., Kinny, P.D.,
657 2017. Interpreting granulite facies events through rare earth element partitioning arrays.
658 *Journal of Metamorphic Geology* 35, 759–775. <https://doi.org/10.1111/jmg.12254>

659 Tera, F., Wasserburg, G.J., 1972. U-Th-Pb systematics in three Appolo 14 basalts and the
660 problem of initial Pb in lunar rocks. *Earth and Planetary Science Letters* 14, 281–304.

661 Valley, J.W., Cavosie, A.J., Ushikubo, T., Reinhard, D.A., Lawrence, D.F., Larson, D.J.,
662 Clifton, P.H., Kelly, T.F., Wilde, S.A., Moser, D.E., Spicuzza, M.J., 2014. Hadean age
663 for a post-magma-ocean zircon confirmed by atom-probe tomography. *Nature*
664 *Geoscience* 7, 219–223. <https://doi.org/10.1038/ngeo2075>

665 Valley, J.W., Reinhard, D.A., Ushikubo, T., Snoeyenbos, D.R., Larson, D.J., Strickland, A.,
666 Cavosie, A.J., Kelly, T.F., Lawrence, D.F., 2015. Nano- and micro-geochronology in
667 Hadean and Archean zircons by atom-probe tomography and SIMS: New tools for old
668 minerals. *American Mineralogist* 100, 1355–1377. [https://doi.org/10.2138/am-2015-](https://doi.org/10.2138/am-2015-5134)
669 5134

670 Verberne, R., Reddy, S.M., Saxey, D.W., Fougereuse, D., Rickard, W.D.A., Plavsa, D.,
671 Agangi, A., Kylander-Clark, A.R.C., 2020. The geochemical and geochronological
672 implications of nanoscale trace-element clusters in rutile. *Geology* XX, 1–5.

673 <https://doi.org/10.1130/g48017.1>

674 Wawrzenitz, N., Krohe, A., Rhede, D., Romer, R.L., 2012. Dating rock deformation with
675 monazite: The impact of dissolution precipitation creep. *Lithos* 134–135, 52–74.

676 <https://doi.org/10.1016/j.lithos.2011.11.025>

677 Wendt, I., Carl, C., 1991. The statistical distribution of the mean squared weighted deviation.
678 *Chemical Geology: Isotope Geoscience Section* 86, 275–285.

679 [https://doi.org/10.1016/0168-9622\(91\)90010-T](https://doi.org/10.1016/0168-9622(91)90010-T)

680 Wetherill, G.W., 1963. Discordant Uranium-Lead Ages II Discordant ages resulting from
681 diffusion of Lead and Uranium. *Journal of Geophysical Research* 68, 2957–2965.

682 Whitehouse, M.J., Kusiak, M.A., Wirth, R., Ravindra Kumar, G.R., 2017. Metallic Pb
683 nanospheres in ultra-high temperature metamorphosed zircon from southern India.
684 *Mineralogy and Petrology* 111, 467–474. <https://doi.org/10.1007/s00710-017-0523-1>

685

686

687

688

689

690

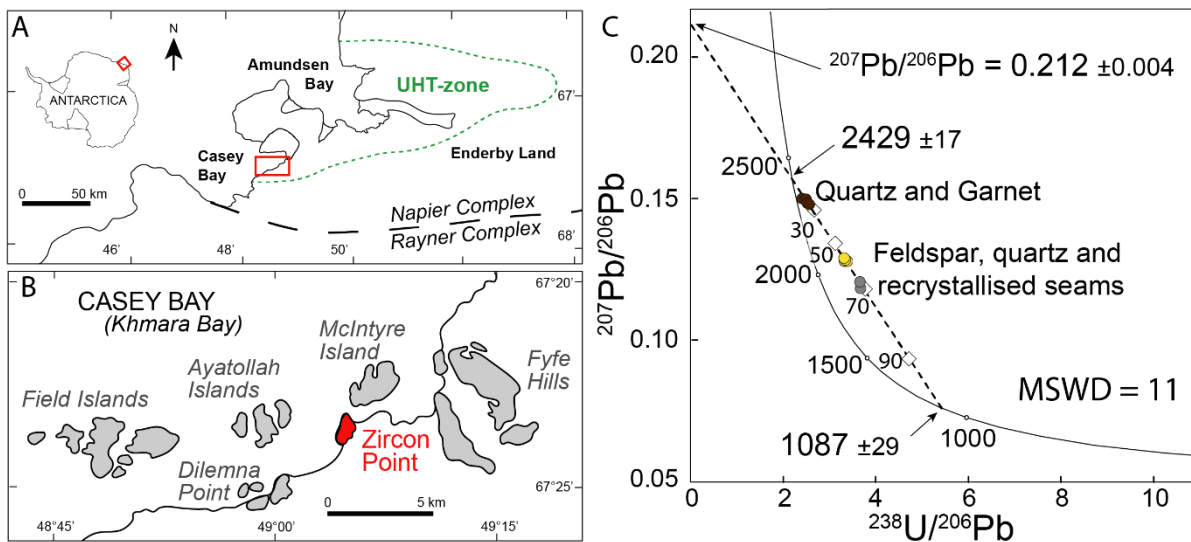
691

692

693

694 **Figures and captions**

695 **1.5-column fitting image** Figure 1. Location map of the sampling area ($\sim 67^{\circ}22'30''$ S and
 696 $49^{\circ}03'45''$ E) and previous geochronological results. A, B: map location of Zircon Point in the
 697 Napier Complex, showing the UHT zone (green dotted line) and the assumed limit between
 698 the Napier and the Rayner complex (black dotted line) from Harley et al. (2019). C: Previous
 699 U–Pb geochronological result on monazite measured by ID-TIMS (multi grain) from Black et
 700 al. (1984). White diamonds along the discordia represent the percentage of Pb loss. Analytical
 701 uncertainties are lower than the size of the symbols.

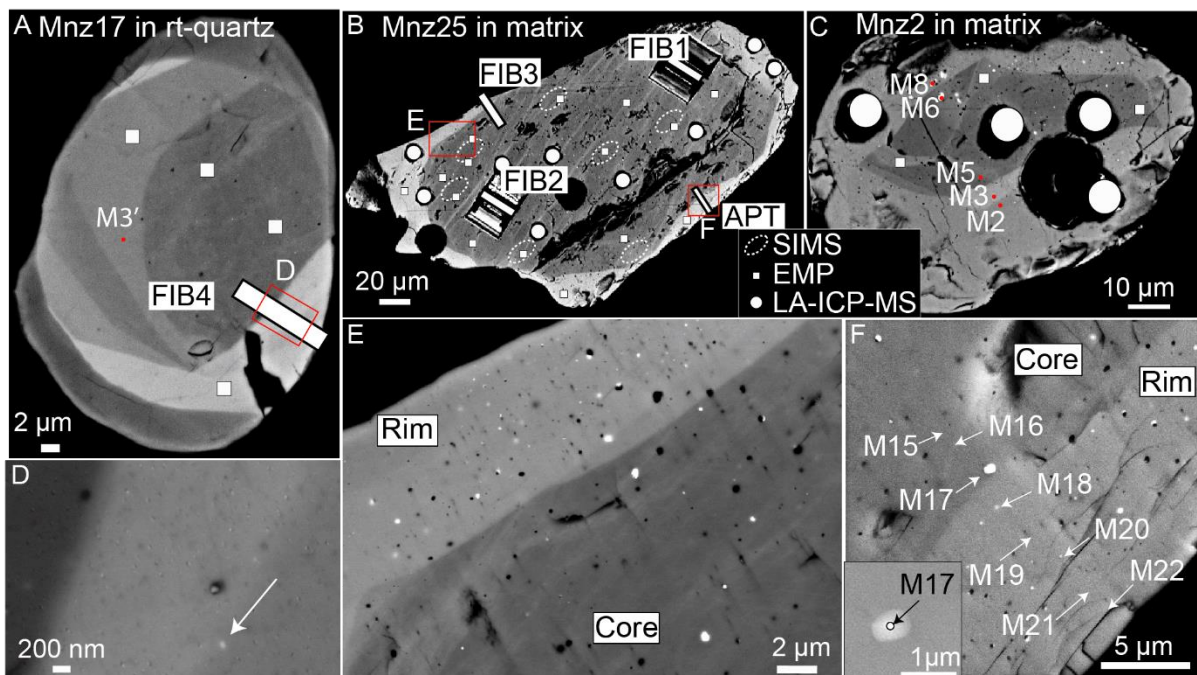


702

703

704

705 **2-column fitting image** Figure 2. Microscale characterization of monazite. A, B, C: High-
 706 contrast BSE SEM imaging of grains Mnz17 (A) hosted in Rt-quartz, Mnz25 (B) and Mnz2
 707 (C) hosted in the quartzo-feldspathic matrix showing a core - rim texture along with NE-SW
 708 oriented bright (high-BSE contrast) linear features traversing the core of Mnz25 (B). The
 709 location of SIMS (white-dashed ellipses), LA-ICP-MS (full white circle) and EMP (white
 710 square) analytical spots are shown (A-C). D-F: High-contrast BSE SEM imaging of selected
 711 region of interest (red rectangles in A and B) displaying bright (high-BSE contrast) and dark
 712 (low-BSE contrast) circular inclusions. Note the smaller size of inclusions in Rt-quartz hosted
 713 monazite (D) compared to quartzo-feldspathic matrix hosted monazite (E-F) as well as the
 714 core-rim feature in (E) with inclusion-poor core and inclusion-rich rim. The location of TEM-
 715 FIB foils (A, B) and APT tips (A, C, F) are also shown with an inset showing the real size of
 716 APT site of interest (F).

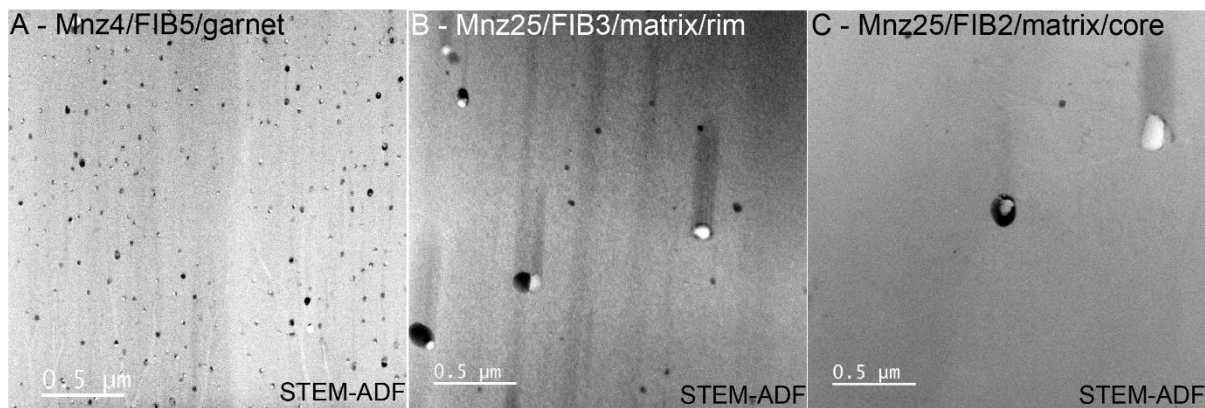


717

718

719

720 **2-column fitting image** Figure 3. Scanning transmission electron microscopy annular dark
721 field images (STEM-ADF) with the same field of view for garnet hosted monazite (A) and
722 quartzo-feldspathic matrix hosted monazite (B, C). Light grey inclusions correspond to
723 distinct crystalline Pb-bearing minerals often polyphased and spatially associated with a dark
724 amorphous Si-rich part. Quartzo-feldspathic matrix hosted monazite display a lower density
725 and larger ($\text{\O} > 50 \text{ nm}$) light Pb-bearing minerals compared to garnet hosted monazite. Note
726 that within quartzo-feldspathic matrix hosted monazite Mnz25, the rim (B) display a higher
727 density of Pb-bearing minerals than the core (C). Vertical dark bands in B correspond to
728 artefacts from FIB polishing (curtaining effects).



729

730

731

744 **1.5-column fitting image** Figure 5. Range of dates depending on the analytical volume.

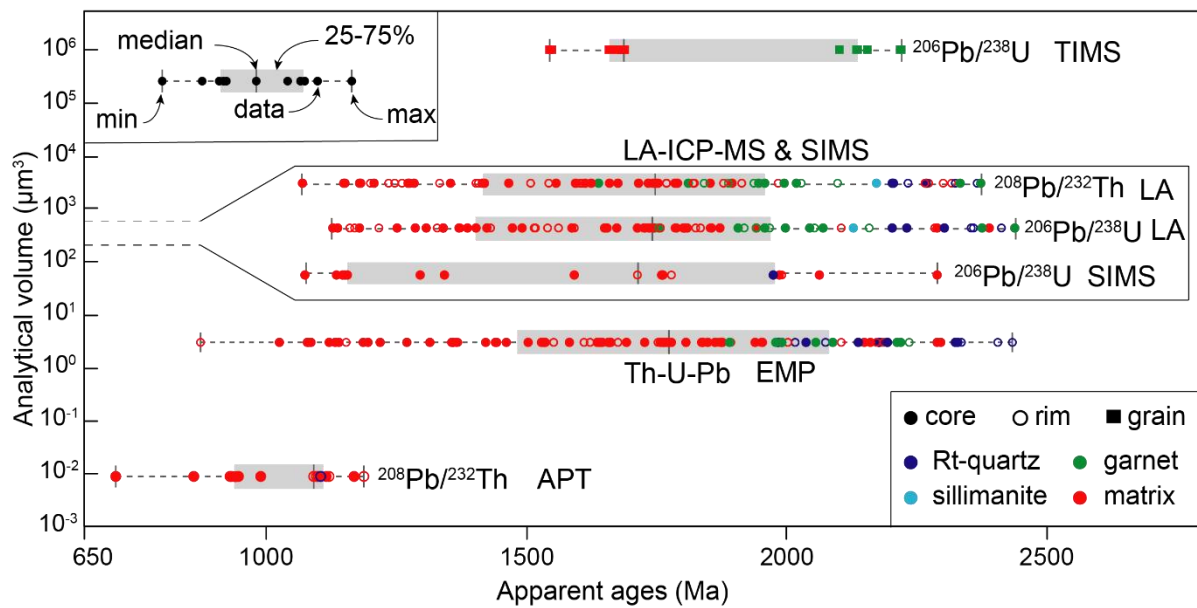
745 Boxplots of dates discriminated by the analytical volume referring to the technique used (ID-

746 TIMS on multi grain from Black et al., 1984, *in-situ* LA-ICP-MS ~ 950 μm^3 , SIMS ~ 600

747 μm^3 , EMP ~ 5 μm^3 and APT < 0.008 nm^3 – this study), the analyzed domain (entire grain,

748 core or rim), and the textural position of the analyzed grain (quartzo-feldspathic matrix =

749 matrix, Rt-quartz, garnet or sillimanite).

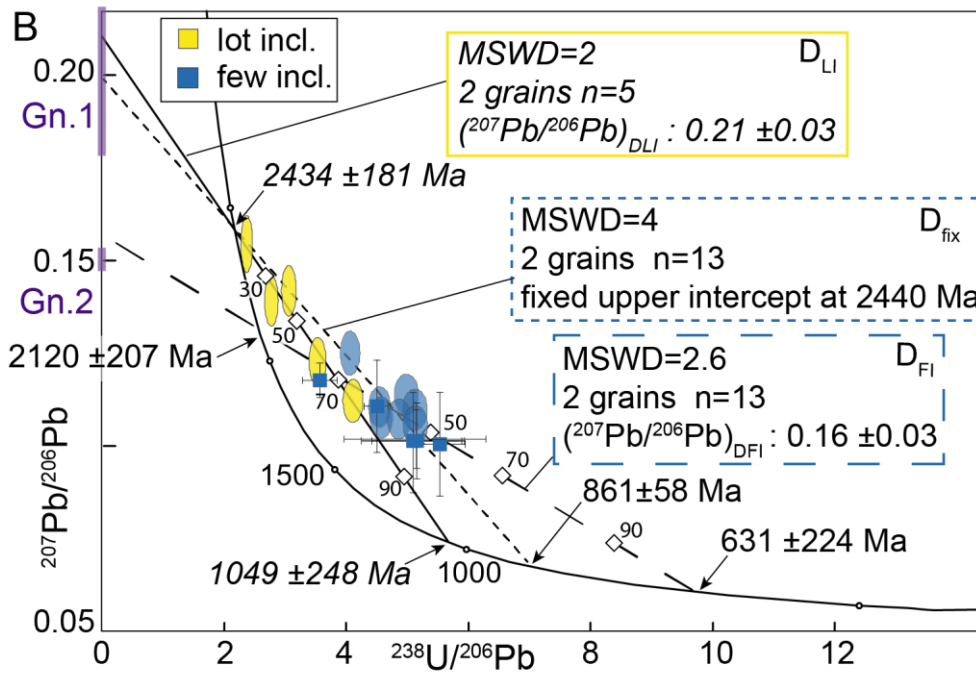
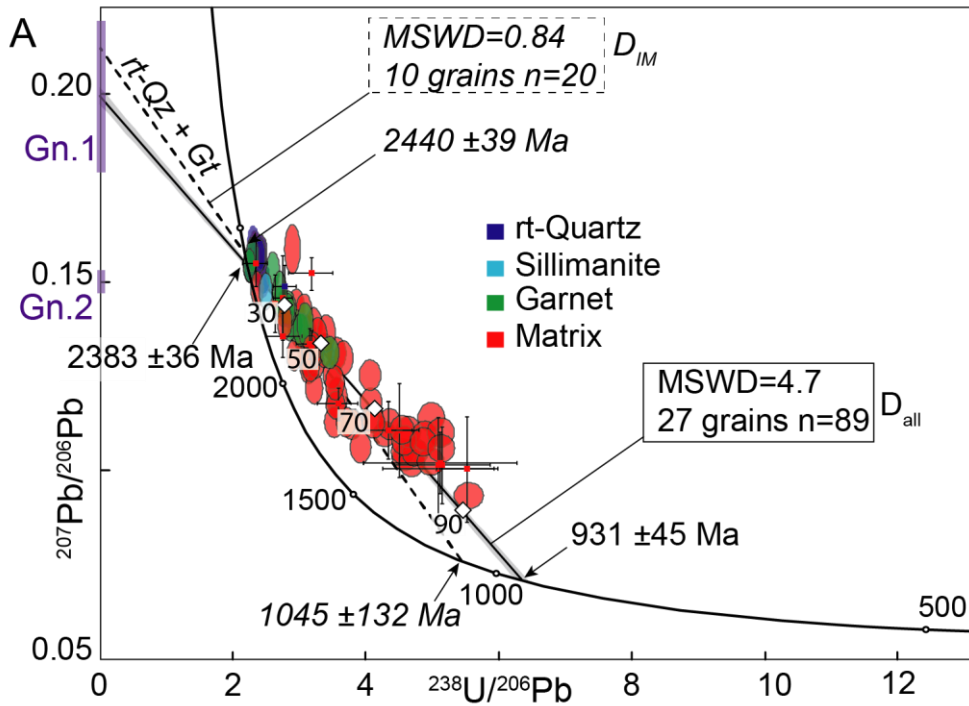


750

751

752

753 **1-column fitting image** Figure 6. Tera-Wasserburg diagram from LA-ICP-MS (ellipses) and
754 SIMS (crosses) U–Pb data denoting 2σ uncertainties. White diamonds along the discordia
755 lines represent the percentage of Pb loss. A: U–Pb data with the full dataset color-coded by
756 host mineral. The discordia line D_{all} (solid) constructed with all data defines an upper
757 intercept of 2383 ± 36 Ma and a lower intercept of 931 ± 45 Ma (MSWD = 4.7). Discordia
758 constructed with data from included monazite in Rt-quartz and garnet, D_{IM} (dashed) lead to an
759 upper intercept of 2440 ± 39 Ma and a lower intercept of 1045 ± 132 Ma (MSWD = 0.84). B:
760 U–Pb data for selected quartzo-feldspathic matrix hosted monazite grains discriminated by the
761 content of galena in the analyzed area. Discordia D_{LI} (solid) is constructed from the galena-
762 rich rim domain analyses and indicate a MSWD = 2, an upper intercept of 2434 ± 181 Ma and
763 a lower intercept of 1049 ± 248 Ma. The isotopic composition of Pb produced in the 2434–
764 1049 Ma time interval is given by the intercept of the $^{207}\text{Pb}/^{206}\text{Pb}$ axis at 0.21 ± 0.03 (2σ).
765 Discordia D_{FI} (large dashed) constructed from the galena-poor core domain analyses indicates
766 a MSWD = 2.6, an upper intercept of 2120 ± 207 Ma, a lower intercept of 631 ± 224 Ma and
767 intercepts the $^{207}\text{Pb}/^{206}\text{Pb}$ axe at 0.16 ± 0.03 (2σ). By fixing the upper intercept (discordia D_{fix} ,
768 small dashed) at 2440 Ma, the lower intercept yields a date of 861 ± 58 Ma (MSWD = 4). The
769 purple boxes are the $^{207}\text{Pb}/^{206}\text{Pb}$ ratios, including the 1σ error, calculated for Gn 1 in M6 and
770 Gn 2 in M17.



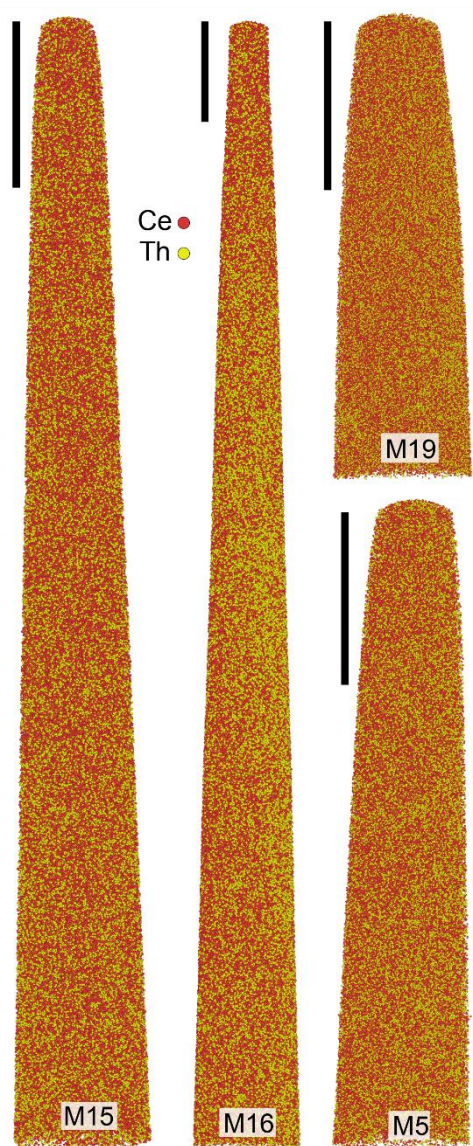
771

772

773

774

775 **1-column fitting image** Figure 7. APT reconstructions of quartzo-feldspathic matrix hosted
776 monazite Mnz25 and Mnz2 in core (M16, M15, M5) and rim (M19) showing Ce and Th
777 atomic distribution. One dot represents one atom. Scale bar = 100 nm. Tips locations are
778 shown on Fig. 2C, F.



779

780

781

782 **1.5-column fitting image** Figure 8. A: Theoretical $^{207}\text{Pb}/^{206}\text{Pb}$ evolution in a monazite
 783 crystallized at 2440 Ma and showing the theoretical value of an isolated reservoir (i.e. galena)
 784 formed at 1045 Ma correlating with $^{207}\text{Pb}/^{206}\text{Pb}$ of Gn 1 within error limits (purple box). B:
 785 Theoretical Pb_1^* component proportion required to form a $^{207}\text{Pb}/^{206}\text{Pb}$ signature of 0.150
 786 considering a $\text{Pb}_1^* + \text{Pb}_2^*$ mixing over time in the studied monazite. C: Theoretical evolution
 787 of $^{238}\text{U}/^{206}\text{Pb}$ and $^{207}\text{Pb}/^{206}\text{Pb}$ ratio in a Tera-Wasserburg diagram for a monazite which
 788 crystallizes at 2440 Ma (t_0) and undergoes two events of Pb^* mobility at 1045 Ma (t_1) and 550
 789 Ma (t_2). D: Schematic Pb^* mobility in monazite; t_0 monazite crystallization free of Pb^* , t_0 to t_1
 790 Pb_1^* growth (red spots), at t_1 x% of Pb_1^* loss at the grain scale along with resetting of
 791 monazite matrix and 1-x% of Pb_1^* isolation as galena. Then t_1 to t_2 Pb_2^* growth in monazite
 792 matrix (green spots). At t_2 Pb^* mixing and isolation as galena in variable proportion of Pb_1^*
 793 and Pb_2^* and t_{actual} theoretical state of the monazite grain.

